Acta Mech 224, 2453–2469 (2013)
DOI 10.1007/s00707-013-0948-5

C. Spieler · M. Kästner · J. Goldmann · J. Brummund · V. Ulbricht

XFEM modeling and homogenization of magnetoactive composites

Received: 15 October 2012 / Revised: 17 December 2012 / Published online: 14 August 2013

Abstract This paper addresses the application of the extended finite element method (XFEM) to the modeling of two-dimensional coupled magneto-mechanical field problems. Continuum formulations of the stationary magnetic and the coupled magneto-mechanical boundary problem are outlined, and the corresponding weak forms are derived. The XFEM is applied to generate numerical models of a representative volume element, characterizing a magnetoactive composite material. Weak discontinuities occurring at material interfaces are modeled numerically by an enriched approximation of the primary field variables. In order to reduce the complexity of the representation of curved interfaces, an element local approach is proposed which allows an automated computation of the level set values. The composite's effective behavior and its coupled magneto-mechanical response are computed numerically by a homogenization procedure. The scale transition process is based on the energy equivalence condition, which is satisfied by using periodic boundary conditions.

1 Introduction

The present study is motivated by the need to develop a multi-scale modeling approach for novel composite materials with magnetically switchable rheological properties. On the microscale, the proposed composite material consists of a polymeric matrix with embedded magnetizable particles as shown in Fig. 1a. Such materials are called magnetorheological or magnetosensitive elastomers. The rheological properties of the composite can be altered by the application of an external magnetic stimulus. This so-called "magnetorheological effect" is caused by magnetic and mechanical interactions between the micron-sized magnetizable particles. During the manufacturing process, before curing the elastomer, the particles are disordered in the absence of an external magnetic induction ($|\mathbf{B}| = 0$). Such a particle configuration is presented by a photomicrograph of a magnetorheological fluid, without an applied magnetic field, in Fig. 1b. A magnetorheological

C. Spieler (✉) · M. Kästner · J. Goldmann · J. Brummund · V. Ulbricht
Institute of Solid Mechanics, Technische Universität Dresden, 01062 Dresden, Germany
E-mail: Christian.Spieler@tu-dresden.de
Tel.: +49-351-46333284
Fax: +49-351-46337061

M. Kästner
E-mail: Markus.Kaestner@tu-dresden.de

J. Goldmann
E-mail: Joseph.Goldmann@tu-dresden.de

J. Brummund
E-mail: Joerg.Brummund@tu-dresden.de

V. Ulbricht
E-mail: Volker.Ulbricht@tu-dresden.de

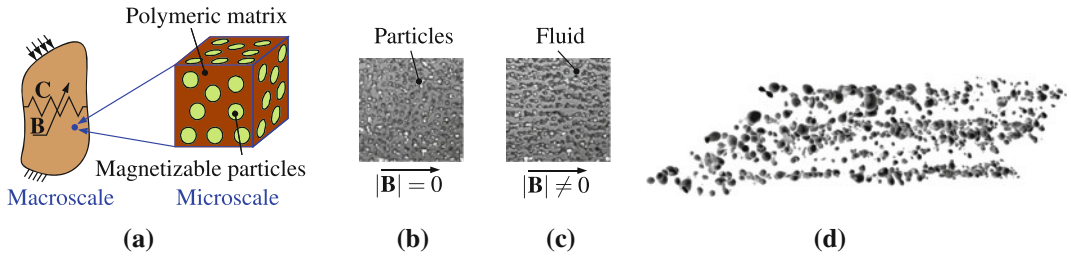

Fig. 1 Composite materials with magnetically switchable properties: **a** hierarchical material structure at two distinct length *scales*; macroscopic stiffness **C** is linked to magnetic induction **B**, **b** photo-micrograph of disordered particles in a magnetorheological fluid without any external magnetic induction ($|\mathbf{B}| = 0$), **c** chain-like clusters of magnetized particles aligned with the external magnetic induction $|\mathbf{B}| \neq 0$ and **d** computed tomography (CT) scan of a magnetorheological elastomer

fluid is chosen for illustrative purposes only and is supposed to demonstrate the movability of the particles in the noncured elastomer. When a magnetic field is applied, forces acting between the individual particles result in the formation of particle clusters, which are aligned with the direction of the magnetic induction **B** (Fig. 1c). If a magnetic field of a certain amount is present during the curing process of the elastomeric matrix, the particles arrange in chain-like structures and keep their position in the polymeric network, see Fig. 1d. These microstructural formations influence the effective magnetic and mechanical properties of the composite.

In order to predict the effective material behavior of the described composite, a modeling approach using a staggered numerical homogenization algorithm based on finite element (FE) simulations of a representative volume element (RVE) is to be presented in this article. There are several techniques to realize the transition between the various length scales, which physically determine the macroscopic material behavior. The group of Billardon considers the level of the magnetic domains, to incorporate the domain evolution and microscopically motivated effects on magnetostriction and magnetization in polycrystalline media, for reversible behavior in [1, 2]. Miehe et al. [3] account for dissipative processes at the grain scale, which results in effective magnetization curves with hysteresis and the butterfly curve (known from ferroelectric materials) for the magnetostrictive strain. In a more phenomenological treatment and with attention to special structural aspects, the effective behavior in the context of small strains is obtained by asymptotic homogenization, for instance in [4] for piezoelectric composites, and in [5] with an exact matrix method for multilayered magneto-electro-thermo-elastic structures. The majority of works are specified on electro-mechanically coupled problems, see for example [6], but can also be applied to magnetoactive materials in a similar manner [7]. Aboudi [8] uses an asymptotic expansion accounting for quadratic terms of the fluctuating fields in electro-magneto-thermo-elastic composites. A variational formulation of the homogenization problem characterizes the macroscopic response of the reversible [9] and dissipative [10] material behavior. An extension to finite strain is proposed by Ponte Castañeda and Galipeau in [11,12] for magnetorheological elastomers limited to nondissipative processes with rigid magnetizable particles of ellipsoidal shape and assuming an "ellipsoidal symmetry". Brigadnov and Dorfmann present a purely phenomenological model for magnetorheological elastomers in [13] without taking any microstructural aspects into account, which results in an isotropic behavior. A continuum formulation of nonlinear magneto-elastostatics is also presented in [14].

For the computational homogenization, a numerical model of the RVE has to be generated which is a particular problem if complex local material structures are considered. In this case, the application of the standard finite element method (FEM) tends to result in an extensive modeling and meshing effort, including problems related to distorted element shapes. The extended finite element method (XFEM) [15,16] offers the possibility to use nonconforming meshes, which do not have to be adapted to internal details, e.g., cracks or material interfaces, of the structure under consideration. The location of discontinuities is independent of the mesh. It is therefore used to model the local heterogeneous material structure of the composite mentioned above.

The paper is organized as follows: In Sect. 2, the stationary magnetic and the magneto-mechanical boundary value problems are presented. By illustrating XFEM in Sect. 3, with a special focus on the *element local* level set computation and the implementation, a modeling strategy for the homogenization problem of Sect. 4 is available. Section 5 provides, in addition to a nonlinear magnetic material model, results concerning the convergence behavior of numerically computed homogenized linear material parameters as well as macroscopic nonlinear magnetization curves. The last part of the results demonstrates the magneto-mechanical coupling effect by analyzing mechanical stresses, which are induced by magnetic loadings. The paper is closed by some concluding remarks and an outlook to necessary future work in Sect. 6.

2 Continuum formulation of the boundary value problems

In this section, the governing equations of the stationary magnetic and the coupled magneto-mechanical boundary value problems (BVP) will be outlined. They describe the local response of the aforementioned magnetoactive composite material. Index notation with respect to a Cartesian frame and the Einstein summation convention is applied. The material body covers the domain Ω, its boundary is labeled $\partial\Omega$ and material points are identified by their position vector $\mathbf{x}$.

2.1 Stationary magnetic boundary value problem

The continuum formulation of the electromagnetic field problem is given by the Maxwell equations [17]. In the stationary case considered here, the equations for the electric and the magnetic field quantities decouple. The corresponding stationary magnetic problem is described by

$$B_{i,i} = 0 \quad \text{and} \tag{1}$$

$$e_{ijk} H_{k,j} = J_i, \tag{2}$$

with the vectors of the magnetic induction $\mathbf{B}$, the magnetic field $\mathbf{H}$ and the free current density $\mathbf{J}$ as well as the third order permutation tensor $\mathbf{e}$. The partial derivative of $(\bullet)$ with respect to the coordinate x_i is abbreviated by $(\bullet)_{,i} := \frac{\partial(\bullet)}{\partial x_i}$. The magnetization $\mathbf{M}$ is related to the magnetic induction, the magnetic field and the permeability of free space μ_0 by

$$B_i = \mu_0 (H_i + M_i). \tag{3}$$

It is essential to state a constitutive relation between two vectors out of $\mathbf{B}$, $\mathbf{H}$ and $\mathbf{M}$ for solving the local magnetostatic BVP. This is achieved for two different materials in Sect. 5.1, where two models, a linear and a nonlinear isotropic constitutive relation, are used for modeling the magnetic material behavior. At a surface of discontinuity Γ_d, the jump conditions

$$[\![B_i]\!] n_i = 0 \quad \text{and} \tag{4}$$

$$e_{ijk} [\![H_k]\!] n_j - K_i = 0, \tag{5}$$

hold for the magnetic induction and the magnetic field. In the equations above, $[\![\psi]\!] = \psi^+ - \psi^-$ is the jump of a physical quantity ψ across Γ_d according to Fig. 2a. Equation (4) mathematically represents the continuity of the normal component of the magnetic induction. If no current density $\mathbf{K}$ acts on Γ_d, the tangential components of the magnetic field have to be continuous according to Eq. (5).

By introducing the magnetic vector potential $\mathbf{A}$ using

$$B_i = e_{ijk} A_{k,j}, \tag{6}$$

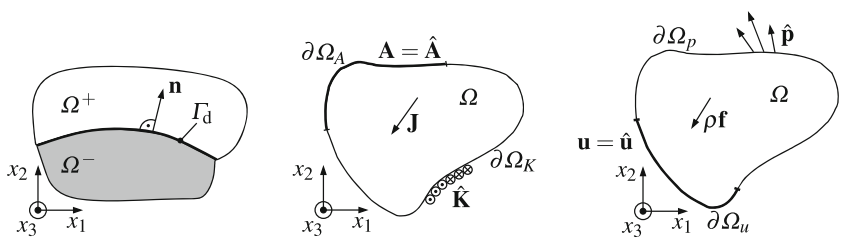

(a) **(b)** **(c)**

Fig. 2 Magnetic and mechanical boundary value problems: **a** surface of discontinuity Γ_d, with associated unit normal vector $\mathbf{n}$, separating the domain Ω of the material body into two domains Ω^+ and Ω^-, **b** magnetic boundary value problem—prescribed vector potential $\hat{\mathbf{A}}$ on $\partial\Omega_A$, surface current $\hat{\mathbf{K}}$ on $\partial\Omega_K$ and current $\mathbf{J}$ in Ω, and **c** coupled magneto-mechanical boundary value problem—prescribed displacements $\hat{\mathbf{u}}$ on $\partial\Omega_u$, surface tractions $\hat{\mathbf{p}}$ on $\partial\Omega_p$ as well as mechanical body force density $\rho\mathbf{f}$ in Ω

Eq. (1) is fulfilled, and only Eq. (2) has to be considered for the solution of the stationary magnetic BVP. An additional condition, for example the Coulomb gauge

$$A_{i,i} = 0, \tag{7}$$

is necessary to obtain a unique solution, because Eq. (6) only defines the rotational part of $\mathbf{A}$. Using this gauge, the essential boundary condition can be formulated by the vector potential $\mathbf{A}$, which serves as the primary variable for the FE implementation. On the part $\partial\Omega_A$ of the external boundary (cf. Fig. 2b), the essential condition

$$A_i = \hat{A}_i \tag{8}$$

is imposed for the ith coordinate of the vector potential. The part of the boundary with the natural boundary condition

$$e_{ijk} H_k n_j = -\hat{K}_i \tag{9}$$

is labeled $\partial\Omega_K$. The prescribed values $\hat{K}_i$ have to represent the effects of any external magnetic field outside the domain Ω and of surface currents $\mathbf{K}$ applied on $\partial\Omega_K$. For the well-posed definition of the boundary conditions, $\partial\Omega_A \cap \partial\Omega_K = \varnothing$ and $\partial\Omega_A \cup \partial\Omega_K = \partial\Omega$ have to be valid for each coordinate direction.

2.2 Coupled magneto-mechanical boundary value problem

The here considered and implemented coupling is weak. This enables deformations caused by static magnetic fields, but the other way around there are no changes in the magnetic variables due to strains or displacements. For the stationary mechanical case, the balances of linear momentum

$$t^{\mathrm{tot}}_{ij,i} + \rho f_j = 0 \tag{10}$$

and angular momentum

$$e_{ijk} t^{\mathrm{tot}}_{jk} = 0 \tag{11}$$

equilibrate the total stress tensor $\mathbf{t}^{\mathrm{tot}}$ and a mechanical body force density $\rho\mathbf{f}$. According to Eq. (11), the total stress tensor is *symmetric*. It can be split into $t^{\mathrm{tot}}_{ij} = t_{ij} + t^{\mathrm{m}}_{ij}$, the sum of a mechanical stress tensor $\mathbf{t}$ and a magnetic stress tensor $\mathbf{t}^{\mathrm{m}}$. This decomposition is not free of arbitrariness. We use the magnetic stress tensor $\mathbf{t}^{\mathrm{m}}$, which is microscopically motivated by de Groot and Suttorp in [18], and specified in this work subsequently. Furthermore, the used decomposition is compatible with phenomenological requirements. In general, i.e., for anisotropic magnetic material behavior, Eq. (11) results in an *unsymmetric* mechanical stress tensor. This can be understood by a couple density, which equals the unsymmetric part of the dyadic product of the magnetization and the magnetic induction $e_{ijk} t^{\mathrm{m}}_{jk} = e_{ijk} M_j B_k$. In this case, it is advantageous, from a numerical point of view,[1] to decompose the symmetric total stress according to [17] into the *symmetric* pseudo-mechanical stress ${}_{\mathrm{E}}\mathbf{t}$ and the pseudo-magnetic stress tensor

$$\hat{t}_{ij} = H_i B_j - B_i M_j - \frac{1}{2}\left(\frac{1}{\mu_0} B_q B_q - 2 M_q B_q\right)\delta_{ij}. \tag{12}$$

The symmetric stress tensors ${}_{\mathrm{E}}\mathbf{t}$ and $\hat{\mathbf{t}}$ are related to the mechanical and the magnetic stresses by

$${}_{\mathrm{E}}t_{ij} = t_{ij} + M_i B_j \quad \text{and} \quad \hat{t}_{ij} = t^{\mathrm{m}}_{ij} - M_i B_j, \tag{13}$$

which does not affect the sum $t^{\mathrm{tot}}_{ij} = {}_{\mathrm{E}}t_{ij} + \hat{t}_{ij}$. As a consequence of the presence of the magnetic stresses, accounted for by $\hat{t}_{ij}$ or t^{m}_{ij}, the jump condition

$$[\![t^{\mathrm{tot}}_{ij}]\!] n_i + p_j = 0 \tag{14}$$

[1] If the constitutive relation for the magnetic material behavior is isotropic, the vectors of magnetization and magnetic induction will be parallel, and thus, no magnetic couple density exists. This preserves the symmetry of all introduced stress tensors. Nevertheless, the formulation of the BVP and the implementation of XFEM are realized by the decomposition $\mathbf{t}^{\mathrm{tot}} = {}_{\mathrm{E}}\mathbf{t} + \hat{\mathbf{t}}$, in order to be able to account for more sophisticated magnetic constitutive relations.

for the traction vector at an internal surface of discontinuity Γ_d is formulated for the total stress tensor. If no mechanical surface load $\mathbf{p}$ is applied on Γ_d, the sum of the mechanical and the magnetic tractions has to be continuous.

There is another part which couples the magnetic and the mechanical BVP. This is expressed by the linear elastic constitutive relation [17]

$$\mathrm{E}t_{ij} = E_{ijkl}\varepsilon_{kl}, \tag{15}$$

formulated with the pseudo-mechanical stress tensor and the fourth order elasticity tensor $\mathbf{E}$. The infinitesimal strain tensor $\boldsymbol{\varepsilon}$ is defined by the linear kinematic relation

$$\varepsilon_{ij} = \frac{1}{2}\left(u_{i,j} + u_{j,i}\right), \tag{16}$$

which connects the strain to the symmetric part of the gradient of the displacement $\mathbf{u}$. From Eq. $(13)_1$, it is obvious that a body which is free of mechanical stresses $\mathbf{t}$ but is magnetized deforms according to Eq. (15).

The magneto-mechanical BVP is completed by suitable boundary conditions according to Fig. 2c. On $\partial\Omega_u$, the essential condition

$$u_i = \hat{u}_i \tag{17}$$

is formulated for the ith coordinate of the displacement vector. The natural boundary condition

$$t_{ij}^{\mathrm{tot}} n_i = \hat{p}_j \tag{18}$$

is prescribed on $\partial\Omega_p$, where the effective surface load $\hat{p}_i$ has to account for any contribution from mechanical and magnetic tractions outside Ω as well as an applied mechanical surface load $\mathbf{p}$. In addition, $\partial\Omega_u \cap \partial\Omega_p = \varnothing$ and $\partial\Omega_u \cup \partial\Omega_p = \partial\Omega$ hold for each coordinate.

3 XFEM modeling of weak discontinuities

Generating numerical models of RVEs is a problem in particular if complex local material structures are considered. In this case, the application of the standard FEM tends to result in an extensive modeling and meshing effort including problems related to distorted element shapes.

XFEM [15,16] offers the possibility to use nonconforming meshes, which do not have to be adapted to internal details, e.g., cracks or material interfaces, of the structure under consideration, see Fig. 3a. Hence, it is used to model the local heterogeneous material structure of the composite mentioned above.

The following section explains the application of XFEM to model discontinuities in the magnetic and the mechanical field problem and to capture the magneto-mechanical coupling due to magnetic loadings and the material behavior.

Originally, XFEM was applied to model strong discontinuities (jumps) in the primary field variables as they occur at a crack [15,19]. The features of XFEM allow for the simulation of crack growth without remeshing as the mesh is independent of the crack topology. In rapid succession, the method has been used to model material interfaces [16,20–22], which represent weak discontinuities in the mechanical BVP. In this context, XFEM and

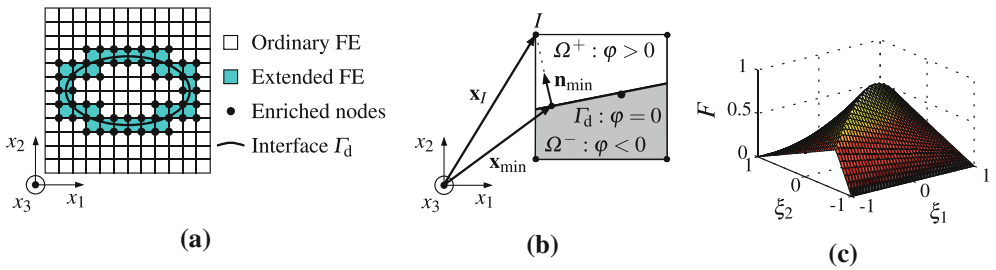

Fig. 3 XFEM modeling of discontinuities: **a** intersection of a surface of discontinuity Γ_d with a regular mesh defines the location of X-elements and the nodes with additional degrees of freedom, **b** computation of level set by signed distance, and **c** modified abs-enrichment F according to [21] depending on local coordinates $\boldsymbol{\xi}$

level sets have been applied to image-based modeling of heterogeneous materials [23,24]. A comprehensive review, concerning the methodological issues of XFEM and various applications, is given for instance in [25].

In this section, an XFEM formulation for weak discontinuities in the stationary magnetic and the coupled magneto-mechanical BVP is developed. The location of the discontinuities is assumed to be identical for the stationary magnetic and the coupled magneto-mechanical field problem. For simplicity and demonstration purposes, only problems homogeneous in the x_3-direction will be considered. In these two-dimensional problems, $A_1 = A_2 = 0$ is an appropriate choice, and the vector potential $\mathbf{A}$ contains only one nonzero component $A_3 = A$. Since there are no gradients in the third direction, the Coulomb gauge (7) is fulfilled and does not have to be considered furthermore.

3.1 XFEM fundamentals

By a *local* enrichment of the FE approximation

$$\boldsymbol{\psi}^{h,\mathrm{XFEM}} = \underbrace{\sum_{I \in \mathcal{N}^{\mathrm{FEM}}} N_I \boldsymbol{\psi}_I}_{\text{FEM}} + \underbrace{\sum_{J \in \mathcal{N}^{\mathrm{enr}}} N_J \boldsymbol{\psi}_J^* F}_{\text{Enrichment}}, \tag{19}$$

of the primary field variables $\boldsymbol{\psi} = \{A,\ \mathbf{u}\}$, where h characterizes the mesh size, discontinuities can be modeled within a nonconforming mesh. The first sum over the product of shape functions N_I and the nodal vector $\boldsymbol{\psi}_I$ of ordinary degrees of freedom at node I represents the standard FE approximation. The enrichment consists of additional degrees of freedom $\boldsymbol{\psi}_J^*$ and an enrichment function F, which accounts for the physical behavior at a surface of discontinuity. By a suitable choice of the enrichment function, strong (jump) and weak (kink) discontinuities in the approximating function can be modeled. The different summation indices in Eq. (19) indicate that only those nodes $J \in \mathcal{N}^{\mathrm{enr}}$ have additional degrees of freedom, whose support contains a discontinuity.

The implementation of XFEM is realized by the definition of special X-elements, which replace the ordinary finite elements intersected by a discontinuity (cf. Fig. 3a). We assume that the *local* enrichment can be restricted to a single element domain, so that no further elements (blending elements [26]) have to be enriched. This has to be ensured by the formulation of the enrichment function F.

In order to represent surfaces of discontinuity within the nonconforming mesh, the standard XFEM procedure is to compute the signed distance

$$\varphi_I = (\mathbf{x}_I - \mathbf{x}_{\min}) \cdot \mathbf{n}_{\min} \tag{20}$$

of the node I with the position vector $\mathbf{x}_I$ to Γ_{d} (Fig. 3b), whereas $\mathbf{n}_{\min}$ is the unit normal vector to the interface at $\mathbf{x}_{\min}$ pointing in the direction of Ω^+. By interpolating the nodal values φ_I using the shape functions N_I

$$\varphi^h = \sum_I N_I \varphi_I = \begin{cases} = 0 & \text{on} \quad \Gamma_{\mathrm{d}} \\ < 0 & \text{in} \quad \Omega^- \\ > 0 & \text{in} \quad \Omega^+ \end{cases}, \tag{21}$$

the values of the discretized level set function φ^h can be computed for every point in the element domain. Hence, the surface of discontinuity Γ_{d} is located by $\varphi^h = 0$. The works of Belytschko et al. [16], Sukumar et al. [20] and Stolarska et al. [27] closely link the concept of implicitly represented internal surfaces by level sets [28] to the XFEM. In addition to the localization of the interface, the level set representation φ^h is used to formulate an enrichment function F. In both, the magnetic and the mechanical field problem, a material interface represents a surface of weak discontinuity. While the potential A and the displacement vector $\mathbf{u}$ have to be continuous in the element, jumps of the magnetic induction $\mathbf{B}$ (tangential to Γ_{d}) and the strain $\boldsymbol{\varepsilon}$ (normal to Γ_{d}) will occur and have to be modeled by the enrichment function. Although the governing equations of both problems are different, the enrichment function

$$F = \sum_I N_I \left|\varphi_I\right| - \left|\sum_I N_I \varphi_I\right| \tag{22}$$

proposed by Moës et al. [21] (Fig. 3c) for modeling weak discontinuities in mechanical BVP is also suitable for the magnetic case. Regarding the implementation of elements with enriched approximations into a commercial

FE code, the so-called "modified abs-enrichment" (22), also known as ridge function, is of special interest, as the influence of additional degrees of freedom at node I is limited to the element domain intersected by a material interface. It can be seen that $F = 0$ for all elements, whose nodal values of the signed distance satisfy $\varphi_I \varphi_J > 0, I \neq J$. Due to this feature of the enrichment, no blending elements are required. The superior convergence of the modified abs-enrichment F over a simple abs-enrichment $\left|\varphi^h\right|$ is reported in [21,26,29].

3.2 Representation of curved interfaces

In order to model complex microstructures using XFEM, a level set representation of the material interfaces has to be obtained, which is an easy task if the shape of the interface can be described by an analytical function, e.g., an ellipse or a sphere. Because analytical expressions for the geometry of interfaces, boundaries, etc., are rarely available for realistic microstructures, robust algorithms are required to convert microstructural information, such as computed tomography (CT) scans, into a level set representation. In a first step, relevant and irrelevant information have to be separated in a process known as image segmentation. Typical algorithms are edge detection [30,31], marching cubes [32,33] or level set based procedures [34–37]. While the latter produces a single level set value for each voxel which can be mapped to the nodes of a finite element mesh and directly used in an XFEM approach as proposed by Legrain et al. [23,24], the other methods will deliver a set of discrete points and their connectivity.

In the following, we will briefly outline the idea of an *element local* level set representation obtained from such a set of discrete points. Compared to the commonly used global level set representation, the computation of nodal level set values is accomplished with respect to a parameter function fitted to the discrete points representing the interface in a single element (Fig. 4). Hence, no information from neighboring elements has to be considered. Since only a set of discrete points is required, the method is applicable to virtually any kind of input data for the interface.

The procedure will be introduced for the case of bilinear quadrilaterals and is subsequently extended to higher-order interface representations, allowing for a significant reduction of the geometric discretization error. A mesh of four regular quadrilaterals, three of them intersected by a discontinuity Γ_d of circular shape according to Fig. 4a, is considered as an illustrative example. The following algorithm is applied element by element:

1. Obtain a set of discrete points defining the interface in the element J, e.g., the points of intersection of the interface Γ_d with the element edges as they are available from marching cube algorithms for image segmentation, indicated by crosses in Fig. 4a.
2. Obtain a linear parameter representation for the straight segment connecting the intersection points.

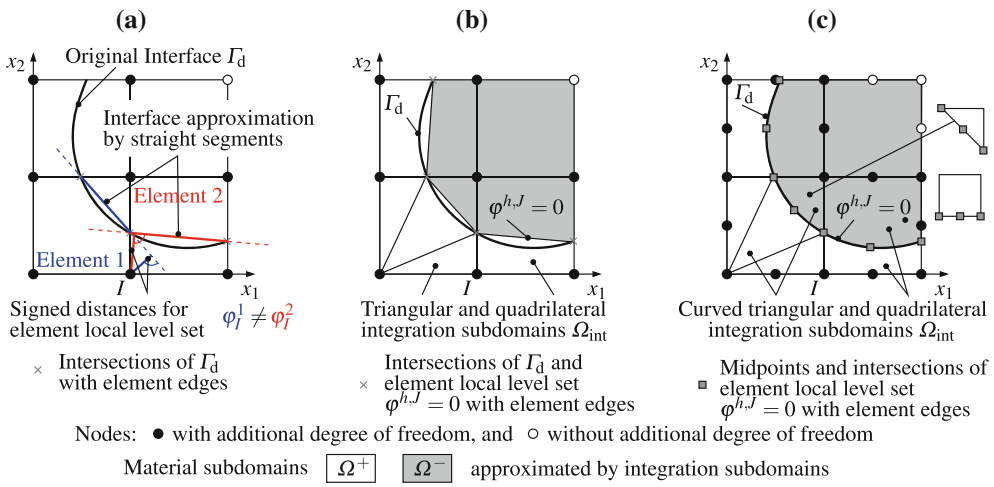

Fig. 4 Element local level set representation of a discontinuity Γ_d: **a** bilinear approximation of original interface by straight segments and computation of different nodal level set values for two adjacent elements, **b** bilinear elementwise level set approximation $\varphi^{h,J} = 0$ and subdivision into integration subdomains, and **c** biquadratic elementwise level set approximation $\varphi^{h,J} = 0$ and subdivision into curved integration subdomains

3. For each node I in element J compute the *element local* nodal level set values φ_I^J as signed distance to the parameter function of step 2 (compare elements 1 and 2 in Fig. 4a). The interface is hence implicitly represented by $\varphi^{h,J} = \sum_I N_I \varphi_I^J = 0$ (Fig. 4b).
4. Subdivide the element domain into triangular and quadrilateral integration subdomains, whereas the vertices of the tessellation are given by the points of intersection and the element nodes.

In the bilinear case of Fig. 4a, b, the interface is, irrespectively of its original shape, converted into straight segments defined by the intersection points of Γ_d with the edges of the regular approximation mesh, which reduces the geometric complexity and facilitates the computation of the nodal level set values. In addition, using this approach, the implicit interface approximation will be consistent with the subdivision of the element domain used for integration purposes as shown in Fig. 4b.

Although the combination of XFEM and level sets originated from linear or bilinear discretizations of the level set function, curved interfaces are of major importance, especially with respect to the generation of complex microstructure models, and have motivated quadratic or higher-order XFEM formulations. Two major approaches to the representation of curved interfaces have been developed. While Cheng and Fries [29], and Kästner et al. [38] use the same order for the interface representation and the approximation of field variables, several authors [39–41] propose to use higher-order approximations of field variables on a coarse mesh, in combination with a discretization of the level set which is defined on a highly refined subgrid, derived from the approximation mesh (background mesh) in the vicinity of the discontinuity.

Following the ideas in [29,38], the previously introduced level set representation can be applied in conjunction with higher-order approximations (Fig. 4c). Compared to the bilinear elements, additional discrete points are required to describe the interface location within the element. In the biquadratic case, for instance, the midpoints of the interface could be used. The nodal values φ_I^J are the signed distances to a higher-order parameter function passing through the discrete points. Hence, the straight edges of the integration subdomains are replaced by curved domains defined by the representation $\varphi^{h,J}$ and the element edges. They are obtained from a geometric map as used for isoparametric FE. In Sect. 5.2, the numerical performance of bilinear and biquadratic approximations is compared in terms of a convergence study.

The quadrature of the weak form can be realized using a subdivision into curved integration subdomains as proposed by [29]. Because curved interfaces result in convex and concave material subdomains, the subdivision into such curved integration subdomains can be problematic for three-dimensional problems. We have therefore proposed and investigated advanced numerical integration techniques for curved interfaces in [38]. All results of the present contribution are obtained using Lasserre's integration [42] in conjunction with the higher-order *element local* level set representations. This integration method offers equal performance, compared to the use of curved integration subdomains, but reduces the complexity of element subdivision.

3.3 X-elements for weak discontinuities in magneto-mechanical problems

Due to the considered weak coupling, which is limited to magnetic loads (12) entering the mechanical equilibrium condition and a constitutive coupling resulting from Eq. (15), the finite element analyses of both problems are performed consecutively, starting with the magnetic boundary value problem. The magnetic loads are then computed from the obtained solution and applied in the mechanical pass.

Starting with the weak form of Eq. (2), the principle of virtual magnetic work,

$$\int_\Omega H_i \delta B_i \,\mathrm{d}V - \int_\Omega J_i \delta A_i \,\mathrm{d}V - \int_{\partial\Omega_K} \hat{K}_i \delta A_i \,\mathrm{d}S = 0, \tag{23}$$

can be derived. The first term represents the internal virtual work, and the latter two are the external virtual works of the currents $\mathbf{J}$ and $\hat{\mathbf{K}}$, respectively.
A weak form of the mechanical equilibrium condition

$$\int_\Omega \left({}_\mathrm{E}t_{ij} + \hat{t}_{ij}\right) \delta\varepsilon_{ij} \,\mathrm{d}V - \int_\Omega \rho f_j \delta u_j \,\mathrm{d}V - \int_{\partial\Omega_p} \hat{p}_j \delta u_j \,\mathrm{d}S = 0 \tag{24}$$

is obtained by Eq. (10) and can be interpreted as the internal virtual work of the pseudo-mechanical and -magnetic stresses and the external virtual work of the mechanical body forces and surface loads accounting for mechanical and magnetic contributions from the exterior of the domain Ω.

The spatial discretization of the domain $\Omega \approx \Omega^h = \bigcup_{I=1}^{n_\mathrm{e}} \Omega_{I\mathrm{e}}$ is performed by a regular mesh with n_e quadrilateral elements, both ordinary isoparametric FE and X-elements with an enriched approximation.

The ordinary isoparametric elements use the same shape functions $N_I(\boldsymbol{\xi})$ for mapping the element geometry from the natural $\boldsymbol{\xi}$ (with $|\xi_i| \leq 1,\ i = 1, 2$) to the physical coordinates $\mathbf{x}$ as well as for the approximation of the primary field variables $\boldsymbol{\psi} = \{A,\ \mathbf{u}\}$ in the element domain Ω_e.

While the mapping of the geometry is retained for the X-elements, the enriched approximation

$$\boldsymbol{\psi}^{h,\text{X-element}}(\boldsymbol{\xi}) = \sum_{I=1}^{n_\mathrm{n}} N_I(\boldsymbol{\xi}) \left[\boldsymbol{\psi}_I + \boldsymbol{\psi}_I^* F(\boldsymbol{\xi})\right] = \underline{\underline{\mathbf{N}}}_{\psi}^*(\boldsymbol{\xi})\, \underline{\boldsymbol{\psi}}_\mathrm{e}^* \tag{25}$$

of the field variables is used to model discontinuities within the element domain. As a consequence, all nodes of the element have a vector of additional degrees of freedom $\boldsymbol{\psi}_I^*$, resulting in a subparametric finite element formulation. Contrasting the isoparametric elements, $\underline{\underline{\mathbf{N}}}_{\psi}^*$ is a matrix containing the shape functions and the products of shape and enrichment functions. The components of the row vector $\underline{\boldsymbol{\psi}}_\mathrm{e}^*$ are the ordinary and additional degrees of freedom of the X-element.

The necessary approximations of the magnetic induction and the strain in the ordinary and the X-elements are given by

$$\underline{\mathbf{B}}^h(\boldsymbol{\xi}) = \underline{\underline{\mathbf{B}}}_A(\boldsymbol{\xi})\underline{\mathbf{A}}_\mathrm{e},\ \underline{\mathbf{B}}^{h,\text{X-element}}(\boldsymbol{\xi}) = \underline{\underline{\mathbf{B}}}_A^*(\boldsymbol{\xi})\underline{\mathbf{A}}_\mathrm{e}^* \quad \text{and} \tag{26}$$

$$\underline{\varepsilon}^h(\boldsymbol{\xi}) = \underline{\underline{\mathbf{B}}}_u(\boldsymbol{\xi})\underline{\mathbf{u}}_\mathrm{e},\ \underline{\varepsilon}^{h,\text{X-element}}(\boldsymbol{\xi}) = \underline{\underline{\mathbf{B}}}_u^*(\boldsymbol{\xi})\underline{\mathbf{u}}_\mathrm{e}^*, \tag{27}$$

whereas the matrices $\underline{\underline{\mathbf{B}}}_A^*$ and $\underline{\underline{\mathbf{B}}}_u^*$ contain the partial derivatives of the shape and enrichment functions with respect to the natural coordinates and account for the mapping of the geometry.

The required element matrices and vectors of the X-elements are obtained from inserting the approximations according to Eqs. (25)–(27) into the corresponding weak forms of the magnetic (23) and the magneto-mechanical BVP (24) given in vector-matrix notation by

$$\int_\Omega \delta\underline{\mathbf{B}}^T \underline{\mathbf{H}}\, \mathrm{d}V - \int_\Omega \delta\underline{\mathbf{A}}^T \underline{\mathbf{J}}\, \mathrm{d}V - \int_{\partial\Omega_K} \delta\underline{\mathbf{A}}^T \hat{\underline{\mathbf{K}}}\, \mathrm{d}S = 0 \quad \text{and} \tag{28}$$

$$\int_\Omega \delta\underline{\boldsymbol{\varepsilon}}^T{}_\mathrm{E}\underline{\mathbf{t}}\, \mathrm{d}V - \int_\Omega \left(\delta\underline{\mathbf{u}}^T \rho\underline{\mathbf{f}} - \delta\underline{\boldsymbol{\varepsilon}}^T \hat{\underline{\mathbf{t}}}\right) \mathrm{d}V - \int_{\partial\Omega_p} \delta\underline{\mathbf{u}}^T \hat{\underline{\mathbf{p}}}\, \mathrm{d}S = 0. \tag{29}$$

The discrete Ritz formulations of the problems in a single X-element,

$$\delta\underline{\mathbf{A}}_\mathrm{e}^{*T} \Bigg\{ \underbrace{\int_{\Omega_\mathrm{e}} \underline{\underline{\mathbf{B}}}_A^{*T} \underline{\underline{\mathbf{C}}}_A \underline{\underline{\mathbf{B}}}_A^*\, \mathrm{d}V}_{\underline{\underline{\mathbf{K}}}_{A,\mathrm{e}}^*} \underline{\mathbf{A}}_\mathrm{e}^* - \underbrace{\int_{\Omega_\mathrm{e}} \underline{\underline{\mathbf{N}}}_A^{*T} \underline{\mathbf{J}}\, \mathrm{d}V - \int_{\partial\Omega_\mathrm{e}} \underline{\underline{\mathbf{N}}}_A^{*T} \hat{\underline{\mathbf{K}}}\, \mathrm{d}S}_{-\underline{\mathbf{P}}_{A,\mathrm{e}}^*} - \underline{\mathbf{J}}_\mathrm{e}^* \Bigg\} = 0 \quad \text{and} \tag{30}$$

$$\delta\underline{\mathbf{u}}_\mathrm{e}^{*T} \Bigg\{ \underbrace{\int_{\Omega_\mathrm{e}} \underline{\underline{\mathbf{B}}}_u^{*T} \underline{\underline{\mathbf{C}}}_u \underline{\underline{\mathbf{B}}}_u^*\, \mathrm{d}V}_{\underline{\underline{\mathbf{K}}}_{u,\mathrm{e}}^*} \underline{\mathbf{u}}_\mathrm{e}^* - \underbrace{\int_{\Omega_\mathrm{e}} \left(\underline{\underline{\mathbf{N}}}_u^{*T} \rho\underline{\mathbf{f}} - \underline{\underline{\mathbf{B}}}_u^{*T} \hat{\underline{\mathbf{t}}}\right) \mathrm{d}V - \int_{\partial\Omega_\mathrm{e}} \underline{\underline{\mathbf{N}}}_u^{*T} \hat{\underline{\mathbf{p}}}\, \mathrm{d}S}_{-\underline{\mathbf{P}}_{u,\mathrm{e}}^*} - \underline{\mathbf{F}}_\mathrm{e}^* \Bigg\} = 0, \tag{31}$$

result from the approximation of the virtual quantities by the same matrices as the field variables by Eq. (25) and their derivatives according to Eqs. (26) and (27). In the equations above, a vector matrix notation of linear magnetic material behavior and the constitutive relation (15) involving the constitutive matrices $\underline{\underline{\mathbf{C}}}_A$ and $\underline{\underline{\mathbf{C}}}_u$ has been used. The vectors $\underline{\mathbf{J}}_\mathrm{e}^*$ and $\underline{\mathbf{F}}_\mathrm{e}^*$ account for discrete nodal loads typically used in FE analyses. Finally, the systems of discrete equations for a single X-element,

$$\underline{\underline{\mathbf{K}}}_{A,\mathrm{e}}^* \underline{\mathbf{A}}_\mathrm{e}^* = \underline{\mathbf{P}}_{A,\mathrm{e}}^* + \underline{\mathbf{J}}_\mathrm{e}^* \quad \text{and} \quad \underline{\underline{\mathbf{K}}}_{u,\mathrm{e}}^* \underline{\mathbf{u}}_\mathrm{e}^* = \underline{\mathbf{P}}_{u,\mathrm{e}}^* + \underline{\mathbf{F}}_\mathrm{e}^*, \tag{32}$$

follow from the argument of arbitrary virtual potentials and displacements. The global systems of equations are obtained by the assembly of the element matrices and vectors, and the incorporation of the boundary conditions.

By using a nonlinear constitutive relation to model the magnetic material behavior, e.g., the Langevin function in Sect. 5.1, the algorithmic tangent modulus and the magnetic field strength have to be provided for an iterative solution of the stationary magnetic BVP.

4 Homogenization approach

In this section, an algorithm for computing the macroscopic magnetic and the coupled magneto-mechanical response of magnetoactive composite materials is presented. The underlying microscopic structure is represented by a two-dimensional RVE of rectangular shape with two pairs of opposing boundaries $\partial\Omega^{I\pm}$, $I = 1, 2$, cf. Fig. 5a. All nodes at the boundary of the discretized model can be grouped into node pairs, which are connected by the two vectors $\Delta\mathbf{x}^I$. Volume averages

$$\langle(\bullet)\rangle := \frac{1}{V_{\mathrm{RVE}}}\int_{\Omega}(\bullet)\,\mathrm{d}V \tag{33}$$

over the RVE domain Ω with the volume V_{RVE} are used to determine macroscopic values, which are labeled by $\bar{(\bullet)}$. Feasible boundary conditions for the RVE problem arise from the Hill-Mandel energy equivalence theorem [43], also known as the macro-homogeneity condition,

$$\bar{H}_i\bar{B}_i = \langle H_i\rangle\langle B_i\rangle = \langle H_i B_i\rangle \quad \text{and} \quad \bar{t}^{\mathrm{tot}}_{ij}\bar{\varepsilon}_{ij} = \langle t^{\mathrm{tot}}_{ij}\rangle\langle\varepsilon_{ij}\rangle = \langle t^{\mathrm{tot}}_{ij}\varepsilon_{ij}\rangle, \tag{34}$$

together with the balance equations (2) and (10), excluding the volume loads $\mathbf{J}$ and $\rho\mathbf{f}$. The basis of the presented scale transition process is the equivalence of the macroscopic energy and the one stored in the heterogeneous microstructure. The macroscopic induction $\bar{\mathbf{B}}$ and the macroscopic strain $\bar{\boldsymbol{\varepsilon}}$ are prescribed as control variables. The boundary conditions for the vector potential and the displacement consist of a linear term and a periodic fluctuation part, whereas the conjugated variables of the tangential magnetic field and the total traction have to be antiperiodic—altogether commonly called *periodic boundary conditions*. The local field problem of the RVE is formulated according to Sect. 2, and a numerical model is generated using XFEM as said above in the context of Sect. 3. Figure 5b schematically shows the nonconforming mesh together with two additional master nodes M^I and a support to prevent rigid body motions. According to [44], periodic boundary conditions are realized by prescribing the potential and the displacement, corresponding to the macroscopic induction and strain state, to only two master nodes which are coupled to the opposing node pairs. The linear or the linearized (for nonlinear magnetic material behavior) system of equations is solved by an elimination procedure and partitioning.

4.1 Effective magnetic response

By choosing the vector potential according to the mentioned periodic boundary conditions

$$A_3 = e_{3pq}\bar{B}_p x_q + \tilde{A}_3, \tag{35}$$

the macro-homogeneity condition $(34)_1$

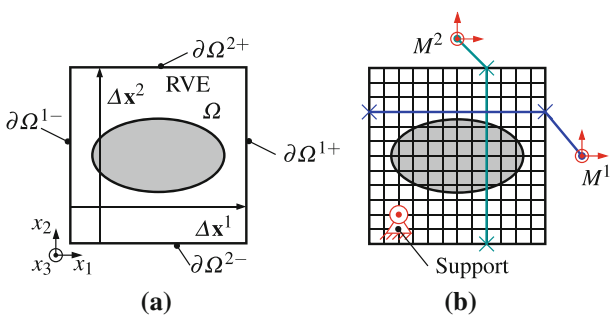

Fig. 5 Two-dimensional representative volume element: **a** pairs of opposing surfaces $\partial\Omega^{I\pm}$ and characteristic vectors $\Delta\mathbf{x}^I$ with $I = 1, 2$, and **b** nonconforming regular XFEM mesh with nodal degrees of freedom coupled to two additional master nodes M^I and support to prevent rigid body motions

$$\frac{1}{V_{\mathrm{RVE}}}\int_{\Omega} H_l B_l \,\mathrm{d}V = \frac{1}{V_{\mathrm{RVE}}}\int_{\partial\Omega} H_l e_{lmn}\left(\delta_{n3} e_{3pq}\bar{B}_p x_q + \delta_{n3}\tilde{A}_3\right) n_m,$$

$$\mathrm{d}S = \frac{1}{V_{\mathrm{RVE}}}\int_{\Omega} H_l \bar{B}_l - H_3\bar{B}_3 + H_l e_{lm3}\tilde{A}_{3,m}\,\mathrm{d}V \tag{36}$$

is fulfilled. The second term on the right-hand side of the equation above vanishes, because we restrict the condition of homogeneity in the x_3-direction to $H_3 = 0$. The last term in Eq. (36) is equal to zero, if an antiperiodic surface current density $K_3^{I+} = -K_3^{I-}$ and a periodic fluctuation of the vector potential $\tilde{A}_3^{I+} = \tilde{A}_3^{I-}$ are assumed. In addition to this fluctuation term Eq. (35) contains a linear part $e_{3pq}\bar{B}_p x_q$.

The macroscopic field strength $\bar{\mathbf{H}}$ can be computed by the volume average (33), which simplifies for the addressed RVE to

$$\bar{H}_k = \frac{1}{V_{\mathrm{RVE}}}\int_{\Omega} H_k \,\mathrm{d}V = \frac{1}{2V_{\mathrm{RVE}}}\int_{\partial\Omega} e_{kmn}e_{qsn}H_q x_m n_s \,\mathrm{d}S = \frac{1}{A_{\mathrm{RVE}}}\sum_{I=1,2} e_{kl3}\Delta x_l^I I_3^I, \tag{37}$$

with the area of the RVE A_{RVE}, the vectors connecting the opposing nodes $\Delta\mathbf{x}^I$ and the master node reaction currents

$$I_3^I = \int_{l^{I+}} e_{3qs}H_q n_s \,\mathrm{d}l, \tag{38}$$

calculated from a one-dimensional boundary integral. The effective magnetization $\bar{\mathbf{M}}$ can be obtained using Eq. (3) in a macroscopic manner with the known values $\bar{\mathbf{B}}$ and $\bar{\mathbf{H}}$.

4.2 Effective magneto-mechanical response

Similar to Eq. (36), it is easy to show that the two-dimensional displacement field

$$u_i = \bar{\varepsilon}_{ij}x_j + \tilde{u}_i \tag{39}$$

satisfies the Hill–Mandel lemma $(34)_2$, together with the condition that the total traction has to be antiperiodic, i.e., $p_i^{I+} = -p_i^{I-}$. The equation above consists of a linear term $\bar{\varepsilon}_{ij}x_j$ and a periodic fluctuation part $\tilde{u}_i^{I+} = \tilde{u}_i^{I-}$. A macroscopic as well as a microscopic state of plane strain are assumed.

With the mechanical master node reaction forces

$$F_j^I = \int_{l^{I+}} t_{ij}n_i \,\mathrm{d}l, \tag{40}$$

one calculates the macroscopic mechanical stress of the RVE by

$$\bar{t}_{ij} = \frac{1}{A_{\mathrm{RVE}}}\sum_{I=1,2}\Delta x_i^I F_j^I, \tag{41}$$

the dyadic product of the characteristic RVE vectors $\Delta\mathbf{x}^I$ and the master node reaction forces divided by the area of the RVE.

5 Demonstration of magneto-mechanical homogenization with XFEM

In this section, the introduced homogenization algorithm together with the local numerical XFEM modeling is validated for one particular periodic microstructure. Furthermore, the nonlinear magnetization behavior of one composite's constituent is modeled. After the definition of the considered microstructure, a convergence study on the effective linear magnetic and linear mechanical properties demonstrates the applicability of the XFEM modeling strategy. Macroscopic magnetization curves with anisotropic effects and mechanical actuation stresses, these are the macroscopic mechanical stresses caused by a magnetic stimulus with no macroscopic deformation $\boldsymbol{\varepsilon} = \mathbf{0}$, are analyzed for three different load cases.

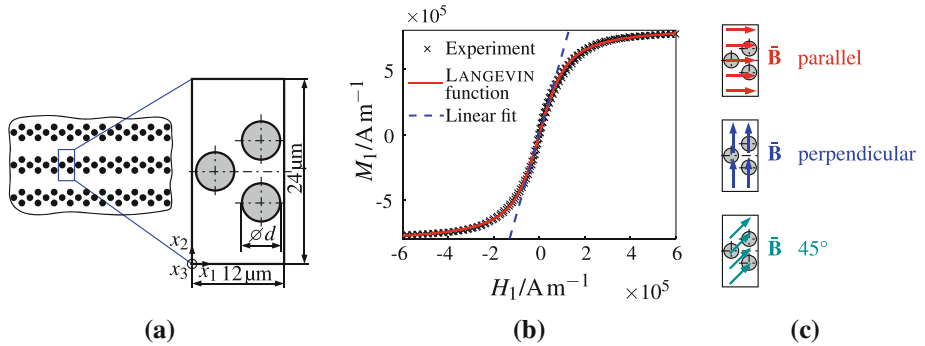

Fig. 6 Idealized periodic microstructure: **a** RVE containing three circular inclusions with diameter d, **b** nonlinear magnetization behavior of BASF CIP CC powder assumed for the circular inclusions—experimental results and models according Eqs. (42) and (43), and **c** three macroscopic magnetic load cases

5.1 Definition of the problem and modeling the nonlinear magnetic material behavior

The considered idealized two-dimensional microstructure is shown in Fig. 6a. Its internal structure is motivated by the chain-like arrangement of magnetizable particles, which is formed due to particle interactions during the curing process of the composite's polymeric matrix with an applied magnetic field (cf. Fig. 1d). The RVE in Fig. 6a contains three circular inclusions. All inclusions are assigned with the material behavior of the carbonyl iron powder BASF CIP CC and have the diameter d. In the x_1–x_2-system, the centers of the inclusions are located at (3; 12) µm, (9; 8) µm and (9; 16) µm.

Some experimental results concerning the magnetic material behavior of the BASF CIP CC are presented in Fig. 6b. For the composite's constituents, it is a convenient choice to postulate the isotropic relation $M_l = \frac{H_l}{H} M(H)$, where $H = \sqrt{H_q H_q}$ and $M = \sqrt{M_q M_q}$. The analyzed material BASF CIP CC exhibits a nonlinear magnetization curve with negligible hysteresis effects, cf. Fig. 6b. Within a group of four reviewed models, the Langevin function [45]

$$M = M_\mathrm{S} \left[\coth(\delta H) - \frac{1}{\delta H} \right] \tag{42}$$

points out to be the most suitable approximation for the phenomenological modeling of the nonlinear magnetic material behavior under consideration. This function has two parameters which have to be determined by experiments, the saturation magnetization M_S and a scaling parameter δ. The result obtained for the BASF CIP CC with $M_\mathrm{S} = 8.4 \times 10^5\ \mathrm{A\,m^{-1}}$ and $\delta = 2.2 \times 10^5\ \mathrm{m\,A^{-1}}$ is plotted in Fig. 6b by a solid line. A linearization of Eq. (42) in the neighborhood of $H = 0$ yields the constant relative permeability

$$\mu_\mathrm{r} = \frac{M_\mathrm{S}\delta}{3} + 1, \tag{43}$$

and Eq. (3) can be rewritten in the simple form $B_l = \mu_0 \mu_\mathrm{r} H_l$, which describes linear isotropic magnetic material behavior. As expected, the dashed line in Fig. 6b, with $\mu_\mathrm{rI} = 7.2$, shows that this approximation is only reasonable for small values of the magnetic field. The composite's elastomeric matrix consists of Wacker Chemie AG Elastosil® RT 745, which is assumed to be nonmagnetizable $\mu_\mathrm{rM} = 1$.

Both constituents are modeled linear elastic according to Eq. (15) with the isotropic parameters Young's moduli $E_\mathrm{I} = 2.1 \times 10^5$ MPa and $E_\mathrm{M} = 0.2$ MPa as well as the Poisson ratios $\nu_\mathrm{I} = 0.3$ and $\nu_\mathrm{M} = 0.4$ for the inclusions (I) and the matrix (M), respectively.

5.2 Convergence study regarding the effective linear magnetic and linear mechanical composite response

At first, the effective magnetic behavior is analyzed using the relative permeabilities $\mu_\mathrm{rI} = 7.2$ and $\mu_\mathrm{rM} = 1$ for the constituents of the RVE. All inclusions have a diameter of $d = 3.8\,\mu\mathrm{m}$, which results in a volume fraction of approximately 12 %. The RVE is meshed with either bilinear or biquadratic elements and six discretizations with 8×16, 16×32 (cf. Fig. 7a), 32×64, 64×128, 128×256 and 256×512 elements. The mesh resolution

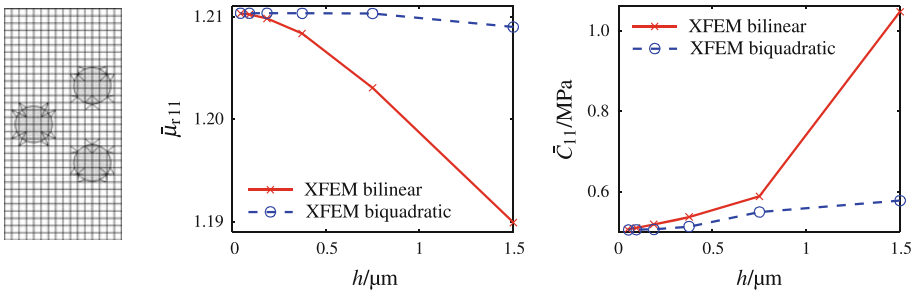

(a) **(b)** **(c)**

Fig. 7 Selected results of a convergence study for the effective material behavior using bilinear and biquadratic elements with different discretization h: **a** meshed RVE with $d = 3.8$ and $h = 0.75\,\mu$m—ordinary FE together with triangular and quadrilateral integration subdomains of the XFE, **b** relative permeability $\bar{\mu}_{r\,11}$, and **c** stiffness $\bar{C}_{11}$

is specified by the size of the element edge h. According to the geometrical arrangement of the circular inclusions, the macroscopic magnetic behavior becomes anisotropic resulting in the second order tensor of effective relative permeability $\bar{\boldsymbol{\mu}}_r$. With the linear relation $\bar{\mathbf{B}} = \mu_0 \bar{\boldsymbol{\mu}}_r \bar{\mathbf{H}}$, the computed macroscopic magnetic field corresponding to Eq. (37) and the prescribed macroscopic magnetic induction, the sought-after tensor of relative permeability is evaluated. To characterize the composite's anisotropic response, two magnetic load cases are defined and solved, one with $\bar{\mathbf{B}}$ parallel to the x_1-axis and the second one parallel to the x_2-direction. In Fig. 7b, the representative component $\bar{\mu}_{r\,11}$ is plotted using either bilinear or biquadratic elements for all six mesh resolutions. A monotonic convergence is observed for both element types, the bilinear and the biquadratic. Even with the coarsest mesh, the results obtained with the higher-order elements produce errors of $<0.2\,\%$. All results lie in between the Reuss [46] $\bar{\mu}^{\mathrm{R}}_{r\,11} = 1.1$ and Voigt bound [47] $\bar{\mu}^{\mathrm{V}}_{r\,11} = 1.7$.

To obtain the effective stiffness matrix $\bar{\mathbf{C}}$, which is the linear mapping between the strain vector and the stress vector, a purely mechanical homogenization ($\mathbf{B} = \mathbf{0}$) is performed under the assumption of plane strain. Three macroscopic states of strain are prescribed to the RVE and are solved numerically, i.e., two uniaxial strain and one shear mode. The RVE's effective linear elastic stiffness matrix is computed from the corresponding macroscopic stresses according to Eq. (41) together with the prescribed strain. The results of the convergence study by means of the component $\bar{C}_{11}$ are plotted in Fig. 7c. It is noticeable that the coarse discretizations produce higher relative errors compared to the effective magnetic behavior at the same resolution. This is due to the large difference between the used Young's moduli of almost six orders of magnitude, the relative permeabilities of both components differ only by the factor 7.2. Such a high stiffness ratio results in relatively stiff element matrices of the X-elements, which is recognizable by the large overestimation with coarse resolutions for both, the bilinear and the biquadratic elements. Again, all values obtained numerically, lie in between the Reuss $\bar{C}^{\mathrm{R}}_{11} = 0.49$ MPa and the Voigt bound $\bar{C}^{\mathrm{V}}_{11} = 3.34 \times 10^4$ MPa. Because the matrix is very soft and has a high volume fraction, compared to the inclusions, together with the geometrical arrangement (inclusions are entirely embedded in the matrix material), the computed results using periodic boundary conditions are close to the Reuss bound, where a homogeneous stress field is assumed.

The magnetic and the mechanical macroscopic properties converge from different directions, cf. Fig. 7b, c. This is because in the macroscopic magnetic material behavior, the tensor of the relative permeability $\bar{\boldsymbol{\mu}}_r$ has the nature of a compliance rather than a stiffness, since $\bar{\mathbf{B}}$ can be interpreted as a kinematic and $\bar{\mathbf{H}}$ as the conjugated kinetic variable.

5.3 Effective magnetization of the composite

The composite's macroscopic magnetic behavior is characterized by effective magnetization curves $\bar{M}(\bar{H})$. In the following, all circular inclusions have a diameter of $d = 5\,\mu$m, resulting in a volume fraction of approximately $20\,\%$, and the RVE is meshed with 49×98 biquadratic elements. Both introduced models for the magnetization are used, the nonlinear according to the Langevin function (42) and the linearized model corresponding to Eq. (43). A macroscopic magnetic induction with an intensity of 2 T is applied to the RVE within 20 increments for three different directions: parallel, perpendicular and under an angle of 45° to the internal chain direction, cf. Fig. 6c. Applying such a high magnetic induction, which is experimentally hardly

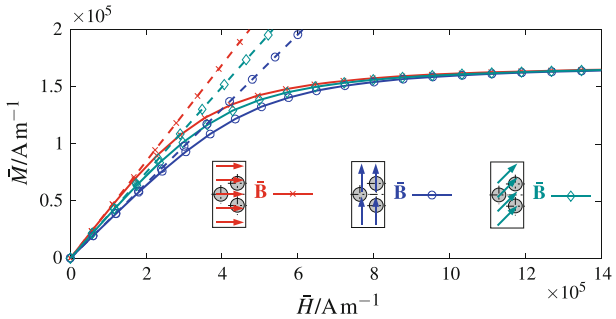

Fig. 8 Numerically computed effective magnetization curves for three different load cases with nonlinear (*solid lines*) and linear (*dashed lines*) behavior of the circular inclusions and a magnetic linear matrix material

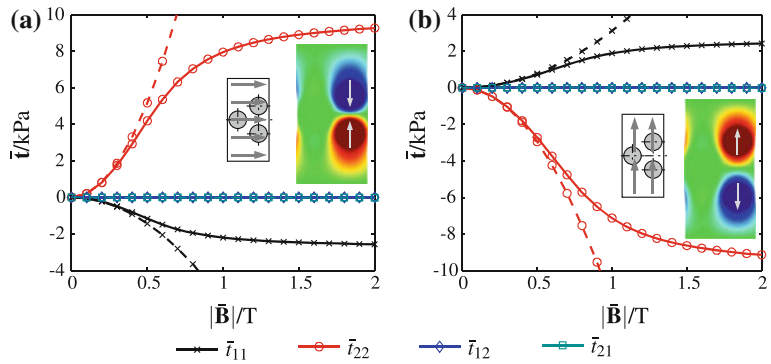

Fig. 9 Macroscopic mechanical actuation stresses for magnetic loading $|\bar{\mathbf{B}}| = 2\text{T}$ within 20 increments and $\bar{\boldsymbol{\varepsilon}} = \mathbf{0}$: **a** macroscopic magnetic induction applied parallel, and **b** perpendicular to the internal chain-like structure. Nonlinear magnetic response of the inclusions is displayed with *solid lines* and the linear approximation with *dashed lines*

achievable without losing the often required homogeneity of the macroscopic field and the essential stationarity, is motivated by discovering the full range of the composite's inherent physical nonlinearity.

The results in Fig. 8 show the obtained effective magnetization curves for the nonlinear magnetic material of the inclusions (solid lines) and the linear approximation (dashed lines). As a consequence of the internal composite structure, the effective magnetic material behavior is anisotropic. This effect decays for strong magnetic fields due to the magnetic saturation characteristic of the circular inclusions in the nonlinear case. For the linearized local material behavior, the magnetization stays anisotropic even for high values of the magnetic field, and the difference to the nonlinear solution increases for rising values of $\bar{H}$.

5.4 Coupled macroscopic magneto-mechanical behavior

The coupled effective magneto-mechanical behavior is analyzed by evaluating mechanical actuation stresses according to Eq. (41). These stresses occur in the coupled magneto-mechanical problem, if the macroscopic deformation is fixed to zero, i.e., $\bar{\boldsymbol{\varepsilon}} = \mathbf{0}$, and the composite is loaded magnetically. As a consequence of the periodic boundary condition expressed by Eq. (39), the RVE is allowed to deform only due to the fluctuation terms.

At first, two load cases are considered with the effective magnetic induction either aligned with or perpendicular to the internal chain-like structure. Again, the macroscopic induction of $|\bar{\mathbf{B}}| = 2\text{T}$ is applied to the RVE within 20 increments. Figure 9a shows the mechanical actuation stresses for the macroscopic magnetic induction aligned with the inner chain-like structure. The small inserted picture of the local displacement field u_2 illustrates that the inclusions lying upon each other are attracted. In this contour plot, red corresponds to positive and blue to negative values of the local u_2-coordinate. Because the macroscopic deformation is set to zero, an expansion of the RVE in the x_1-direction is prevented, which is reflected by a negative actuation stress $\bar{t}_{11} < 0$. In the x_2-direction, the attraction of the inclusions is compensated by a tensile stress $\bar{t}_{22} > 0$. In accordance to [12], the initial behavior of the actuation stresses versus the magnetic induction is quadratic.

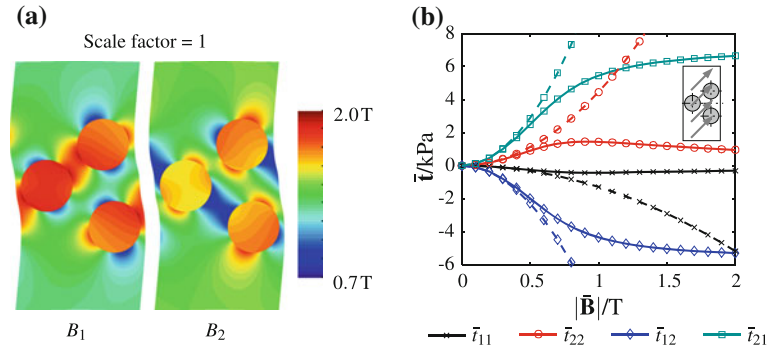

Fig. 10 Magnetic loading $|\bar{\mathbf{B}}| = 2\text{T}$ with an angle of 45° and $\bar{\boldsymbol{\varepsilon}} = \mathbf{0}$: **a** local magnetic induction of deformed RVE, and **b** macroscopic mechanical actuation stresses with the nonlinear (*solid lines*) and linear (*dashed lines*) magnetic material behavior of the inclusions

This can also be understood by Eq. (12), as the pseudo-magnetic stress $\hat{\mathbf{t}}$ depends quadratically on the magnetic field variables and is applied as a load in the weakly coupled magneto-mechanical problem. For $|\mathbf{B}| \gtrsim 0.6\text{T}$, the saturation becomes dominant in the nonlinear case, but in the linearized regime ($\mu_{\text{rI}} = \text{const.}$) the behavior remains quadratic in $|\bar{\mathbf{B}}|$. If the macroscopic induction is applied perpendicular to the inner structure, the circular inclusions move away from each other, cf. Fig. 9b. Consequently, the actuation stresses $\bar{t}_{11} > 0$ and $\bar{t}_{22} < 0$ equilibrate the stresses corresponding to the local deformation field. Again, the initial dependence is quadratic in $|\bar{\mathbf{B}}|$, and then, saturation becomes relevant. The plotted shear stress components $\bar{t}_{12}$ and $\bar{t}_{21}$ are almost zero for the linear and the nonlinear magnetic case and both loading directions.

The last results shown in Fig. 10 correspond to the macroscopic induction applied with an angle of 45°. In Fig. 10a, the contour plots of the local magnetic induction with a sigmoidal deformed RVE are displayed. The actuation stresses in Fig. 10b are qualitatively different from the stresses discussed for the parallel and the perpendicular magnetic field. Here, the normal stress components $\bar{t}_{11}$ and $\bar{t}_{22}$ are smaller than the shear stresses $\bar{t}_{12}$ and $\bar{t}_{21}$. An essential aspect of the results is that the macroscopic mechanical stress tensor is unsymmetric with $\bar{t}_{12} < 0$ and $\bar{t}_{21} > 0$. Both shear stress components equilibrate a macroscopic torque, which acts counterclockwise on the structure, since the magnetic induction is not applied in parallel to the principal axis of the composite. The internal chain-like structure of the composite, cf. Fig. 6a, intends to rotate and align to the external magnetic stimulus. Hence, this causes a macroscopic torque acting on the composite. Again, the initial behavior is quadratic in $|\bar{\mathbf{B}}|$ for the nonlinear magnetic model and quadratic over the whole range of $|\bar{\mathbf{B}}|$ for the linear approximation.

6 Conclusion

We have presented one of the first applications of XFEM to magnetic and coupled magneto-mechanical BVP. By using XFEM for the discretization of a RVE, a homogenization problem for analyzing the macroscopic response of magnetoactive composite materials is numerically solved. An element local approach has been developed, which allows for an automated computation of the level set values and also ensures the compatibility of the level set representation and the integration subdomains. We proved the convergence of bilinear and biquadratic approximations with mesh refinement, regarding the effective linear magnetic and linear mechanical material behavior. Based on magnetization experiments of carbonyl iron powder, a nonlinear and isotropic material model was adapted and compared to a linearized approximation. The analyzed microstructure exhibits a mechanical and a magnetic anisotropy. In general, the latter results in an unsymmetric effective mechanical stress tensor. Actuation stresses for three different magnetic loading directions are found to be in qualitative agreement with experiments on magnetorheological elastomers. Our model predicts an elongation of the composite, if the magnetic stimulus is applied parallel to the chain-like clusters of magnetizable particles.

The methods developed and applied in this work are to be extended to finite strain, to account for large deformations of the matrix material. In the same context, the deformation update of the structure should enable a coupling back to the stationary magnetic BVP.

Acknowledgments This project (ECEMP-B4; SAB: 13854/2379) is funded by the European Union and the Free State of Saxony. We also want to thank Dohmen, E., Hufenbach, W. from TU Dresden, Institute of Lightweight Engineering and Polymer

Technology, for the CT image of a magnetorheological elastomer (Fig. 1d), and Adam, F., Borin, D., Odenbach, S. from TU Dresden, Institute of Fluid Mechanics, for the experimental characterization of the magnetization behavior (Fig. 6b).

References

1. Buiron, N., Hirsinger, L., Billardon, R.: A multiscale model for magneto-elastic couplings. J. Phys. IV France **9**, Pr9-187–Pr9-196 (1999)
2. Daniel, L., Hubert, O., Buiron, N., Billardon, R.: Reversible magneto-elastic behavior: a multiscale approach. J. Mech. Phys. Solids **56**(3), 1018–1042 (2008)
3. Miehe, C., Kiefer, B., Rosato, D.: An incremental variational formulation of dissipative magnetostriction at the macroscopic continuum level. Int. J. Solids Struct. **48**(13), 1846–1866 (2011)
4. Saha, G.C., Kalamkarov, A.L., Georgiades, A.V.: Asymptotic homogenization modeling and analysis of effective properties of smart composite reinforced and sandwich shells. Int. J. Mech. Sci. **49**(2), 138–150 (2007)
5. Kim, J.Y.: Micromechanical analysis of effective properties of magneto-electro-thermo-elastic multilayer composites. Int. J. Eng. Sci. **49**(9), 1001–1018 (2011)
6. Schröder, J.: Derivation of the localization and homogenization conditions for electro-mechanically coupled problems. Comput. Mater. Sci. **46**(3), 595–599 (2009)
7. Hassan, E.M., Kalamkarov, A.L., Georgiades, A.V., Challagulla, K.S.: An asymptotic homogenization model for smart 3D grid-reinforced composite structures with generally orthotropic constituents. Smart Mater. Struct. **18**(7), 075006 (2009)
8. Aboudi, J.: Micromechanical analysis of fully coupled electro-magneto-thermo-elastic multiphase composites. Smart Mater. Struct. **10**(5), 867–877 (2001)
9. Tang, T., Yu, W.: Micromechanical modeling of the multiphysical behavior of smart materials using the variational asymptotic method. Smart Mater. Struct. **18**(12), 125026 (2009)
10. Miehe, C., Rosato, B., Kiefer, D.: Variational principles in dissipative electro-magneto-mechanics: a framework for the macro-modeling of functional materials. Int. J. Numer. Methods Eng. **86**(10), 1225–1276 (2011)
11. Ponte Castañeda, P., Galipeau, E.: Homogenization-based constitutive models for magnetorheological elastomers at finite strain. J. Mech. Phys. Solids **59**(2), 194–215 (2011)
12. Galipeau, E., Ponte Castañeda, P.: The effect of particle shape and distribution on the macroscopic behavior of magnetoelastic composites. Int. J. Solids Struct. **49**(1), 1–17 (2012)
13. Brigadnov, I.A., Dorfmann, A.: Mathematical modeling of magneto-sensitive elastomers. Int. J. Solids Struct. **40**(18), 4659–4674 (2003)
14. Vu, D.K., Steinmann, P.: Material and spatial motion problems in nonlinear electro- and magneto-elastostatics. Math. Mech. Solids **15**(2), 239–257 (2010)
15. Moës, N., Dolbow, J., Belytschko, T.: A finite element method for crack growth without remeshing. Int. J. Numer. Methods Eng. **46**(1), 131–150 (1999)
16. Belytschko, T., Moës, N., Usui, S., Parimi, C.: Arbitrary discontinuities in finite elements. Int. J. Numer. Methods Eng. **50**(4), 993–1013 (2001)
17. Eringen, A.C., Maugin, G.A.: Electrodynamics of Continua I. Springer, New York (1990)
18. Groot, S.R.de , Suttorp, L.G.: Foundations of Electrodynamics. North-Holland, Amsterdam (1972)
19. Daux, C., Moës, N., Dolbow, J., Sukumar, N., Belytschko, T.: Arbitrary branched and intersecting cracks with the extended finite element method. Int. J. Numer. Methods Eng. **48**(12), 1741–1760 (2000)
20. Sukumar, N., Chopp, D., Moës, N., Belytschko, T.: Modeling holes and inclusions by level sets in the extended finite element method. Comput. Methods Appl. Mech. Eng. **190**(46–47), 6183–6200 (2001)
21. Moës, N., Cloirec, M., Cartraud, P., Remacle, J.F.: A computational approach to handle complex microstructure geometries. Comput. Methods Appl. Mech. Eng. **192**(28–30), 3163–3177 (2003)
22. Kästner, M., Haasemann, G., Ulbricht, V.: Multiscale XFEM-modelling and simulation of the inelastic material behaviour of textile-reinforced polymers. Int. J. Numer. Methods Eng. **86**(4–5), 477–498 (2011)
23. Legrain, G., Cartraud, P., Perreard, I., Moës, N.: An X-FEM and level set computational approach for image-based modelling: application to homogenization. Int. J. Numer. Methods Eng. **86**(7), 915–934 (2011)
24. Lian, W.D., Legrain, G., Cartraud, P.: Image-based computational homogenization and localization: comparison between X-FEM/levelset and voxel-based approaches. Comput. Mech. **51**(3), 279–293 (2013)
25. Fries, T.P., Belytschko, T.: The extended/generalized finite element method: an overview of the method and its applications. Int. J. Numer. Methods Eng. **84**(3), 253–304 (2010)
26. Fries, T.P.: A corrected XFEM approximation without problems in blending elements. Int. J. Numer. Methods Eng. **75**(5), 503–532 (2008)
27. Stolarska, M., Chopp, D.L., Moës, N., Belytschko, T.: Modelling crack growth by level sets in the extended finite element method. Int. J. Numer. Methods Eng. **51**(8), 943–960 (2001)
28. Osher, S., Fedkiw, R.P.: Level set methods: an overview and some recent results. J. Comput. Phys. **169**(2), 463–502 (2001)
29. Cheng, K.W., Fries, T.P.: Higher-order XFEM for curved strong and weak discontinuities. Int. J. Numer. Methods Eng. **82**(5), 564–590 (2010)
30. Marr, D., Hildreth, E.: Theory of edge detection. Proc. R. Soc. Lond. B Biol. **207**, 187–217 (1980)
31. Canny, J.: A computational approach to edge detection. IEEE T. Pattern Anal. **8**, 679–698 (1986)
32. Lorensen, W.E., Cline, H.E.: Marching cubes: a high resolution 3D surface construction algorithm. Comput. Graph. **21**, 163–169 (1987)
33. Newman, T.S., Yi, H.: A survey of the marching cubes algorithm. Comput. Graph. **30**, 854–879 (2006)
34. Ibanez, L., Schroeder, W., Ng, L., Cates, J.: The ITK Software Guide, 2nd edn. (2005) Kitware, Inc. ISBN 1-930934-15-7, http://www.itk.org/ItkSoftwareGuide.pdf

35. Li, C., Xu, C., Gui, C., Fox, M.D.: Distance regularized level set evolution and its application to image segmentation. IEEE T. Image Process. **19**(12), 3243–3254 (2010)
36. Shi, Y., Karl, W.: A fast level set method without solving PDEs. IEEE Int. Conf. Acoust. Speech Signal Process. **2**, 97–100 (2005)
37. Roberts, M., Packer, J., Costa Sousa, M., Mitchell, J.R.: A work-efficient GPU algorithm for level set segmentation. High Perform. Graph. (HPG '10), 123–132 (2010)
38. Kästner, M., Müller, S., Goldmann, J., Spieler, C., Brummund, J., Ulbricht, V.: Higher-order extended FEM for weak discontinuities—level set representation, quadrature and application to magneto-mechanical problems. Int. J. Numer. Methods Eng. **93**(13), 1403–1424 (2013)
39. Dréau, K., Chevaugeon, N., Moës, N.: Studied X-FEM enrichment to handle material interfaces with higher order finite element. Comput. Methods Appl. Mech. Eng. **199**(29–32), 1922–1936 (2010)
40. Legrain, G., Chevaugeon, N., Dréau, K.: High order X-FEM and levelsets for complex microstructures: Uncoupling geometry and approximation. Comput. Methods Appl. Mech. Eng. **241–244**, 172–189 (2012)
41. Moumnassi, M., Belouettar, S., Béchet, E., Bordas, S.P.A., Quoirin, D., Potier-Ferry, M.: Finite element analysis on implicitly defined domains: An accurate representation based on arbitrary parametric surfaces. Comput. Methods Appl. Mech. Eng. **200**(5–8), 774–796 (2011)
42. Mousavi, S.E., Sukumar, N.: Numerical integration of polynomials and discontinuous functions on irregular convex polygons and polyhedrons. Comput. Mech. **47**(5), 535–554 (2011)
43. Hill, R.: On constitutive macro-variables for heterogeneous solids at finite strain. Proc. R. Soc. Lond. A **326**, 131–147 (1972)
44. Haasemann, G., Kästner, M., Ulbricht, V.: Multi-scale modelling and simulation of textile reinforced materials. CMC-Comput. Mater. Con. **3**(3), 131–145 (2006)
45. Smith, R.C.: Smart Material Systems—Model development. SIAM Frontiers in Applied Mathematics, Philadelphia (2006)
46. Reuss, A.: Berechnung der Fließgrenze von Mischkristallen auf Grund der Plastizitätsbedingung für Einkristalle. Z. Angew. Math. Mech. **9**(1), 49–58 (1929)
47. Voigt, W.: Über die Beziehung zwischen den beiden Elasticitätsconstanten isotroper Körper. Ann. Phys. **274**(12), 573–587 (1889)